

## Supporting Information

### **Lotus seedpod-inspired electrocatalytic interlayer synthesized via ultrafast Joule heat treatment: overcoming polyiodide shuttle and enhancing redox kinetics in high-areal-capacity aqueous zinc-iodine batteries**

#### **Experimental Procedures**

##### **Synthesis of Fe-Ni@ACC:**

The activated carbon cloth (ACC) was used as current collector, which was sonicated in deionized water, alcohol in sequence and then heated in hydrochloric acid at 80 °C for 1h to remove impurities. Typically, 25 mmol Fe(acac)<sub>3</sub> and 25 mmol NiCl<sub>2</sub>·6H<sub>2</sub>O were dissolved into 100 mL ethanol, respectively. Subsequently, the solutions were stirred together and directly drop-cast onto the ACC at a loading of approximately 120 μL cm<sup>-2</sup>, then allowed to dry at room temperature. In general, ethanol-based solutions result in more uniform loading (and particle dispersion) owing to improved wettability to ACC. These precursors loaded with ACC were used directly for the ultrafast high-temperature (UHT) treatment technology. After synthesis, the carbon cloth was collected and designated as Fe-Ni@ACC. The sample was also prepared by using the same procedure in the absence of metal salts and named Pristine ACC.

##### **Electrochemical Measurements:**

The hydrochloric acid - treated ACC (with a diameter of 6 mm) was used as the

current collector. The cathode was prepared by mixing activated carbon (YP50F) and Polyvinylidene fluoride with a weight ratio of 9:1 in N-Methyl pyrrolidone solvent, which then was coated on ACC and kept at 80°C overnight in a vacuum oven. The calculated mass loading of activated carbon in the final cathode is about 12 mg. Generally, the thickness of the cathode affected the loading amount of active substances and the ion diffusion path. A thicker cathode could accommodate more active substances, thus increasing the capacity. The cells were assembled in CR2032-type coin cells using Fe-Ni@ACC, ACC coated with activated carbon, 0.5 M aqueous ZnSO<sub>4</sub> and 1 M KI, Zn foil (with a diameter of 16 mm) and glass fiber (Whatman® GF/D Glass microfiber filters) as interlayer, cathode, electrolyte, anode, and separator, respectively. The galvanostatic charge/discharge (GCD) tests were carried out by using Neware BTS test system. Cyclic voltammetry (CV) tests were recorded by CHI 730E electrochemical workstation and Autolab PGSTAT-302N instrument.

### **Theoretical calculation:**

This work was performed using the Vienna Ab-initio Simulation Package (VASP) and Density Functional Theory (DFT).<sup>1,2</sup> The Projector Augmented Wave (PAW)<sup>3</sup> method and the Generalized Gradient Approximation (GGA)<sup>4</sup> were employed to describe the electron exchange-correlation energy using the PBE functional, with a D3 dispersion correction added.<sup>5</sup> The plane-wave basis set cutoff energy was set to 500 eV. In order to study the effects of different materials on the binding energy of iodine species ( $I^-$ ,  $I_2$ ,  $I_3^-$ ,  $I_5^-$ ), corresponding single-component models of FeNi alloy, Fe, Ni metal, carbon cloth and ionic species ( $I^-$ ,  $I_2$ ,  $I_3^-$ ,  $I_5^-$ ) were optimized using the Conjugate

Gradient method. The total energy convergence criterion for electron relaxation was set to  $1.0 \times 10^{-5}$  eV, and the convergence criterion for ion relaxation was 0.02 eV/Å. The strong correlation effects for d or f electrons were corrected using the DFT+U approach. The U-J values for Fe, Ni were set to 2.0 eV, 2.5 eV respectively. The Gamma k-point mesh was set to  $3 \times 3 \times 1$ . The adsorption energy was calculated using the formula:  $E_{\text{ads}} = E_{\text{AB}} - E_{\text{A}} - E_{\text{B}}$ , where  $E_{\text{ads}}$  is the adsorption energy,  $E_{\text{AB}}$  is the total energy of the optimized structure for  $\text{I}^-/\text{I}_2/\text{I}_3^-/\text{I}_5^-$  adsorbed on the surface (FeNi alloy or metals or carbon cloth),  $E_{\text{A}}$  is the energy of the isolated  $\text{I}^-/\text{I}_2/\text{I}_3^-/\text{I}_5^-$ , and  $E_{\text{B}}$  is the energy of the surface. The actual iodine catalytic reaction kinetics involves the joint effects of the catalyst and the support, thus the structures of Fe-Ni on graphene-like carbon host, Fe on graphene-like carbon host, and Ni on graphene-like carbon host were used to calculate the Gibbs free energies ( $\Delta G$ ) of Fe-Ni@ACC, Fe@ACC, and Ni@ACC, respectively.  $\Delta G = E_{\text{total}} + E_{\text{ZPE}} - TS$ , where  $E_{\text{total}}$  and  $E_{\text{ZPE}}$  refer to the total energy and zero-point energy calculated by DFT, and TS represents the entropic contribution.

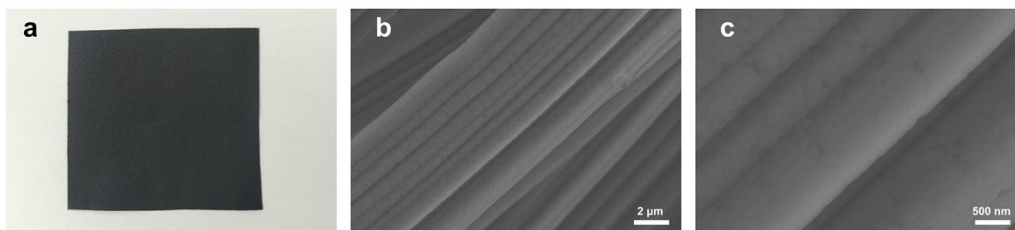


**Figure S1.** (a) Digital image and (b-c) SEM images of ACC, showing uniform nanofiber sizes and an open network structure.

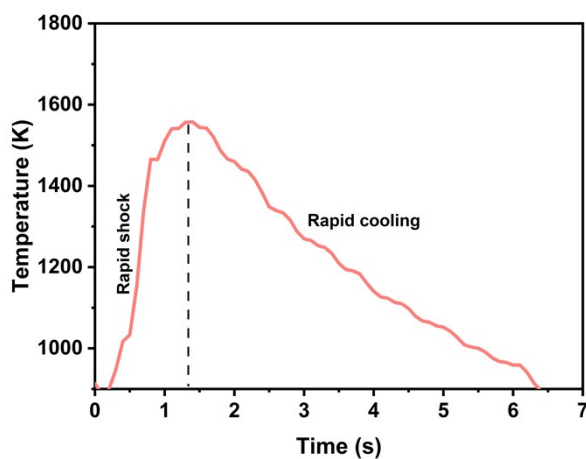


**Figure S2.** Variation of temperature with time during UHT.

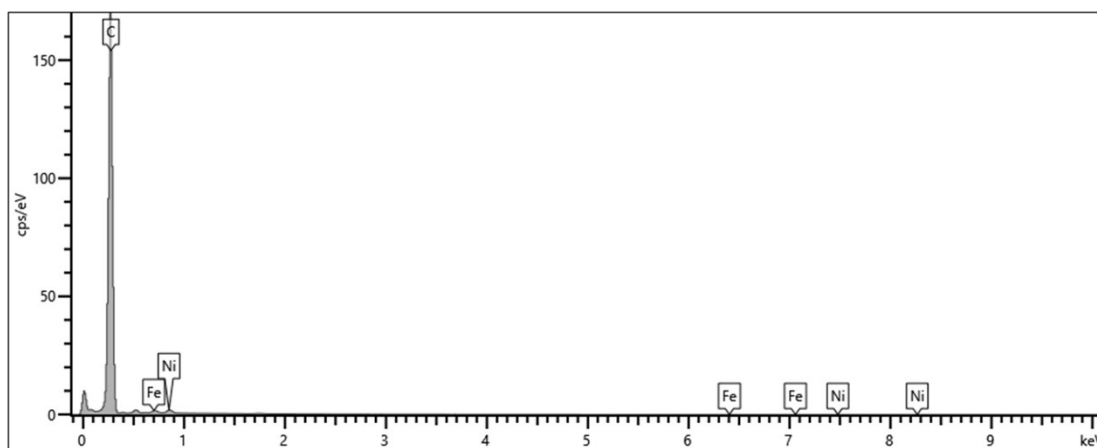


**Figure S3.** EDX of Fe-Ni@ACC synthesized. The content of FeNi is approximately 5 atom% according to the spectrum.

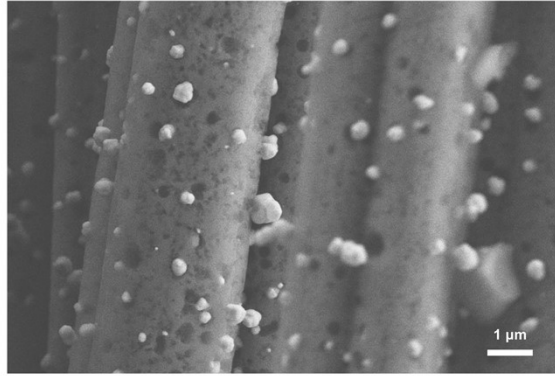


**Figure S4.** SEM image of FeNi alloy on ACC synthesized by heating at 1000 °C for 4h. FeNi alloy is scattered on ACC. The FeNi alloy has a particle size of approximately 1.5 μm and aggregates severely.

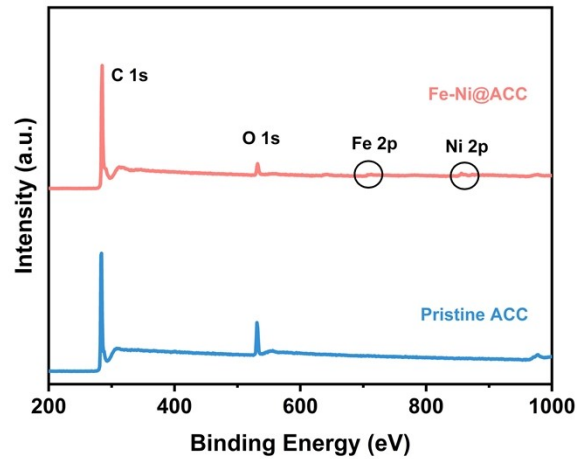


**Figure S5.** XPS survey spectra of Fe-Ni@ACC and Pristine ACC.

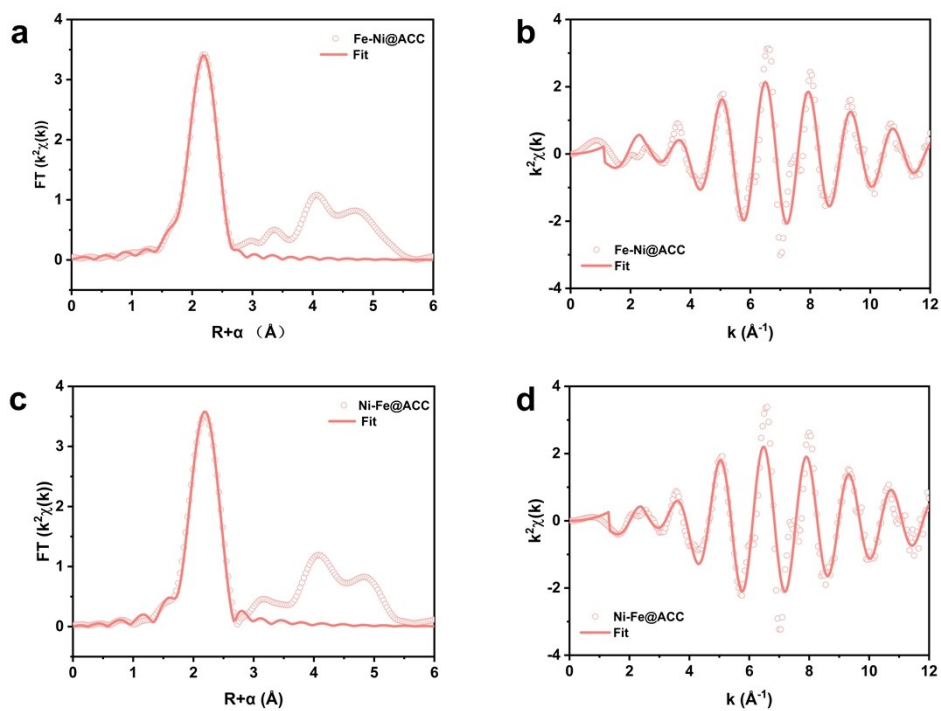


**Figure S6.** (a) Fe K-edge (c) Ni K-edge EXAFS (circles) and the fitting curve (line) for Fe-Ni@ACC, are shown in  $k^2$ -weight R-space. (b, d) The corresponding k-space fitting curves.

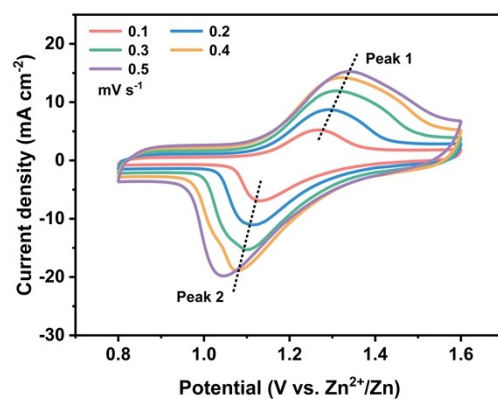


**Figure S7.** CV curves of Pristine ACC at different scan rates.

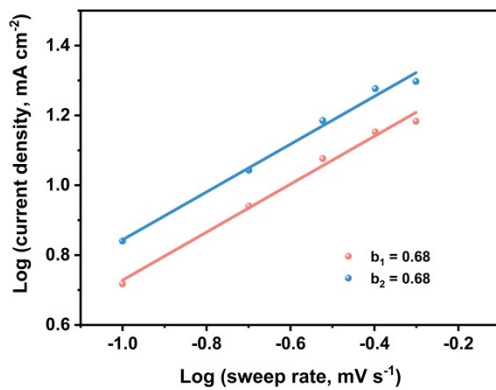


**Figure S8.** Log  $i$  versus log  $v$  plots of the cathodic and anodic current response at the two peaks shown in CV curves of Figure S7.

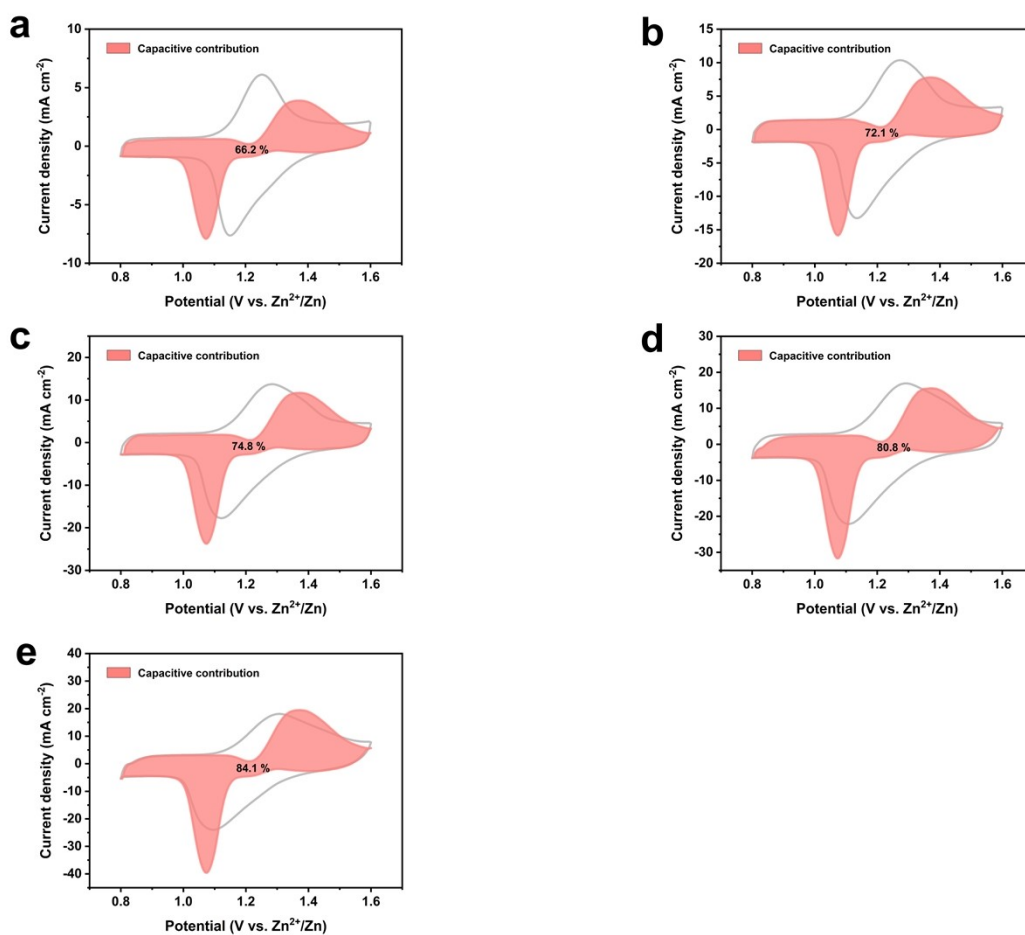


**Figure S9.** Estimated capacitive contributions at scan rates of 0.1, 0.2, 0.3, 0.4 and 0.5  $\text{mV s}^{-1}$ .

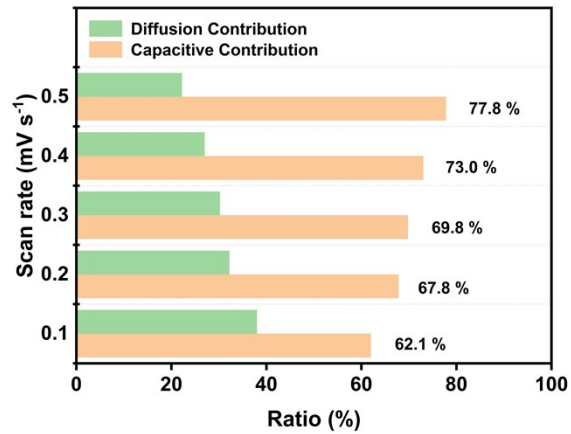


**Figure S10.** Capacitive contributions of Pristine ACC calculated at various scan rates.

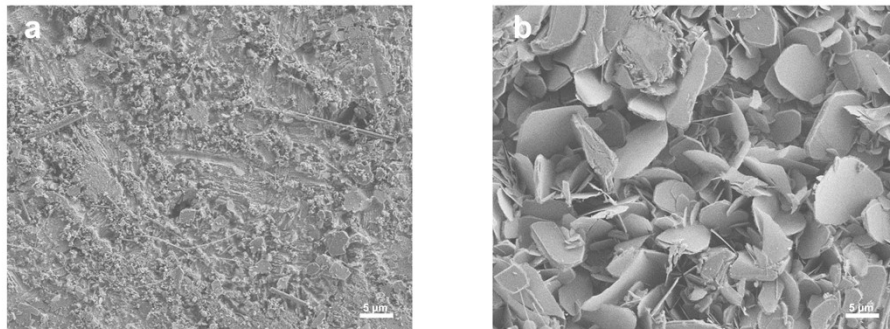


**Figure S11.** SEM images of (a) Fe-Ni@ACC and (b) Pristine ACC interlayers after cycle at 5 C.

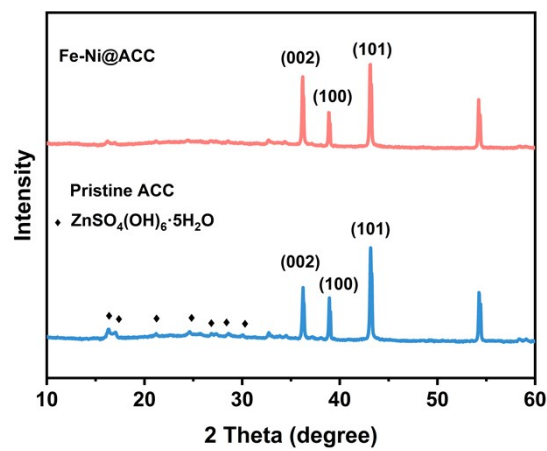


**Figure S12.** The XRD profiles of cycled Zn anodes for Zn-I<sub>2</sub> batteries with Fe-

Ni@ACC and Pristine ACC.

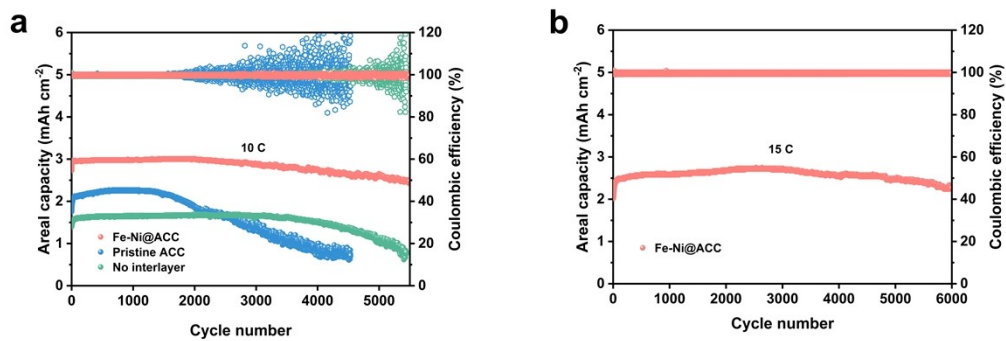


**Figure S13.** Cyclic performance of Zn-I<sub>2</sub> batteries under high rates. (a) The cyclic performance of Zn-I<sub>2</sub> batteries using Fe-Ni@ACC, Pristine ACC and No interlayer at 10 C and (b) 15 C.

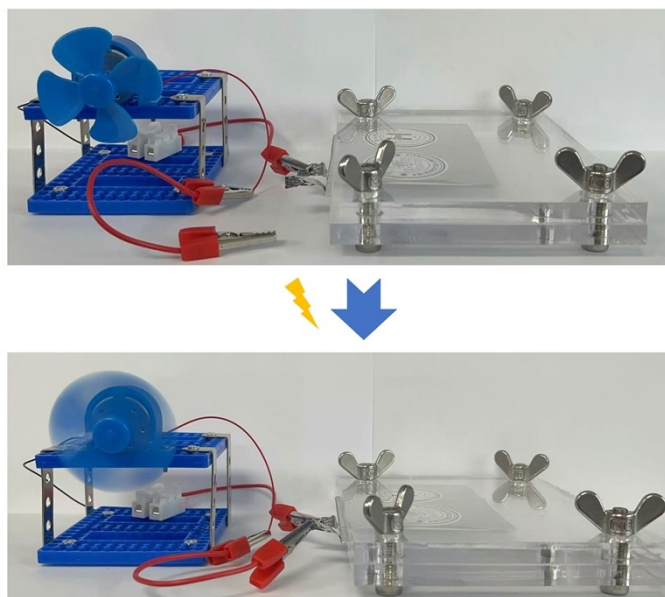


**Figure S14.** The fan is powered by the pouch cell.

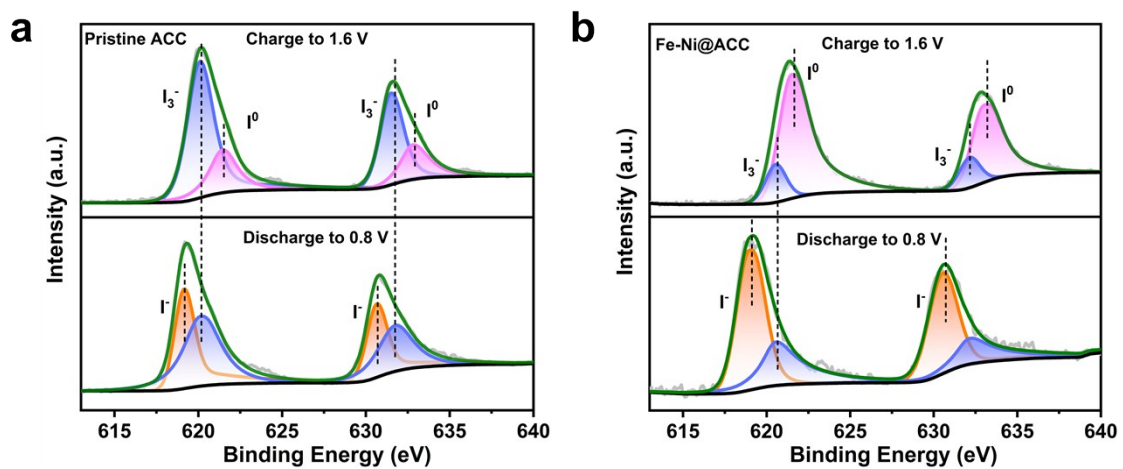


**Figure S15.** High-resolution I 3d XPS spectra of (a) Pristine ACC and (b) Fe-Ni@ACC at fully charged and discharged states.

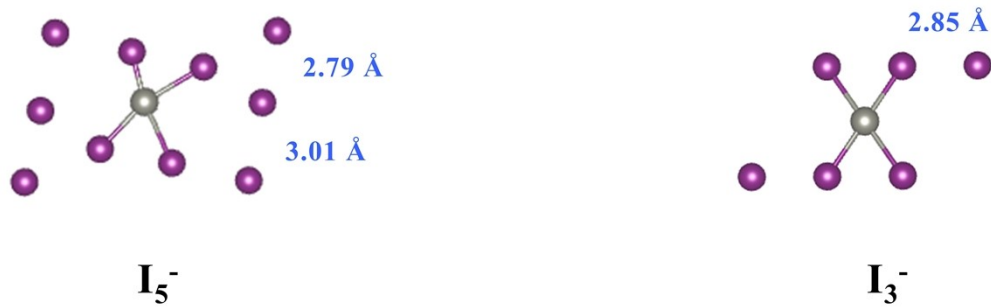


**Figure S16.** The models and I-I bond length of  $I_5^-$  and  $I_3^-$  respectively.

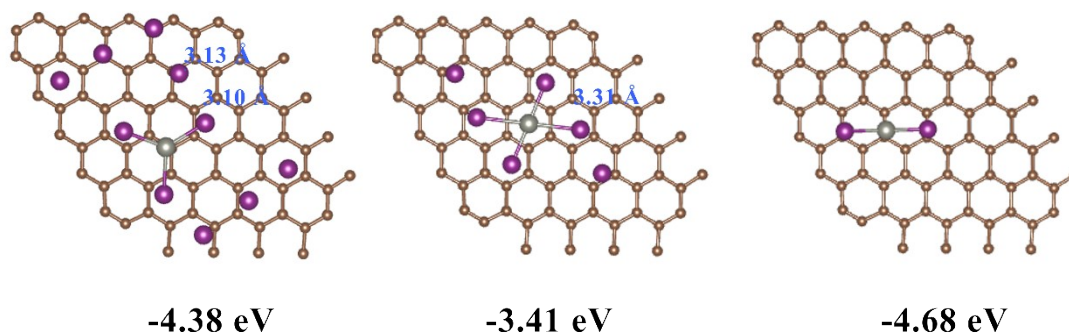


**Figure S17.** The models, adsorption energy and I-I bond length of  $I_5^-$ ,  $I_3^-$ ,  $I^-$  adsorbed on the surface of Pristine ACC, respectively.

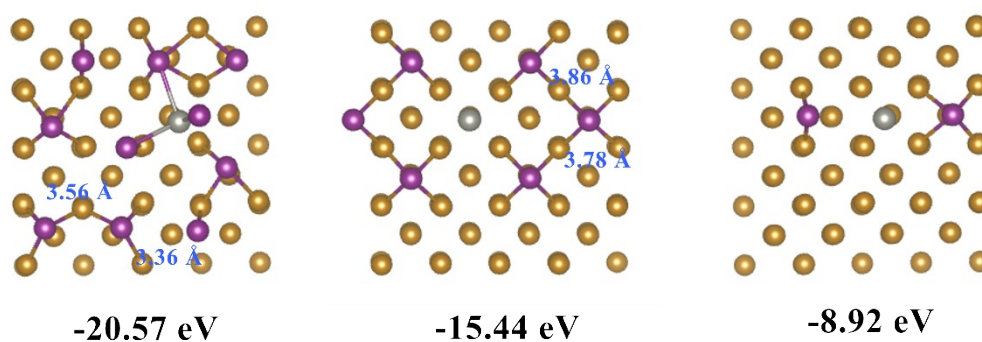


**Figure S18.** The models, adsorption energy and I-I bond length of  $I_5^-$ ,  $I_3^-$ ,  $I^-$  adsorbed on the surface of Fe metal, respectively.

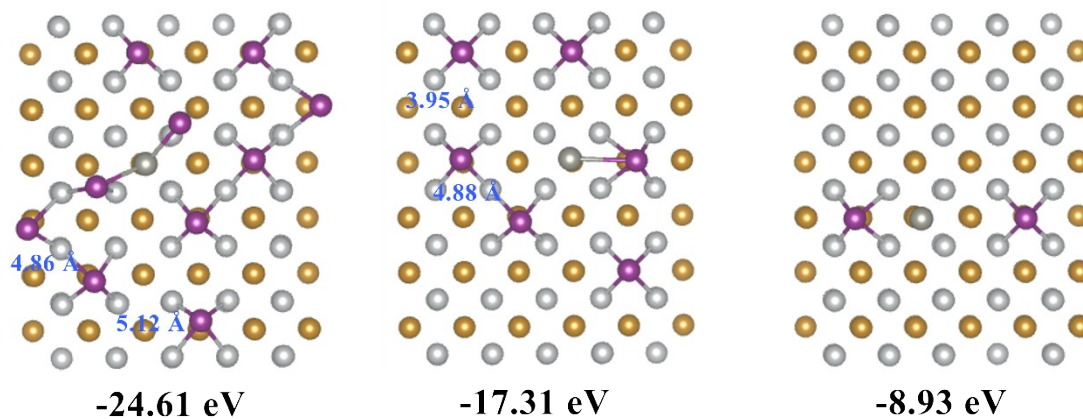


**Figure S19.** The models, adsorption energy and I-I bond length of  $I_5^-$ ,  $I_3^-$ ,  $I^-$  adsorbed on the surface of Fe-Ni alloys, respectively.

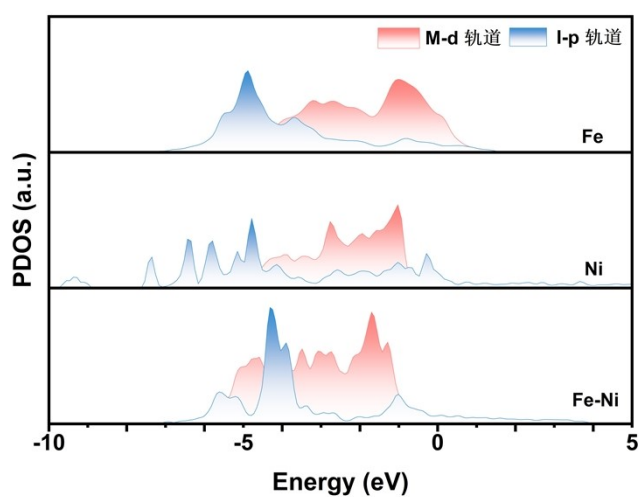


**Figure S20.** PDOS of the p orbital of I and d orbital of metal.

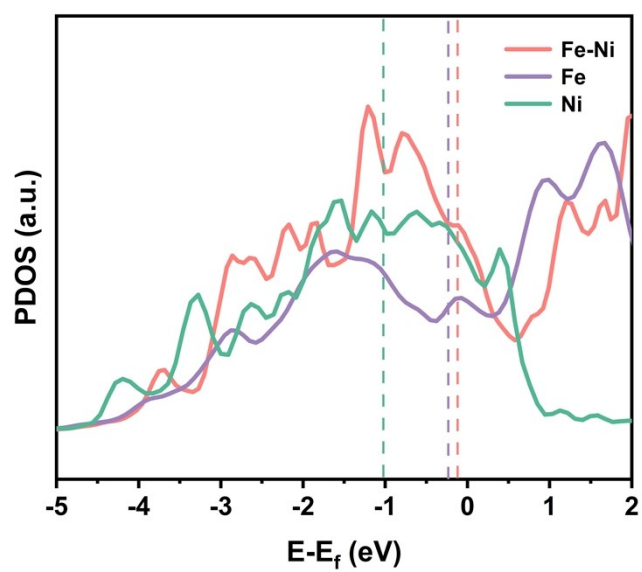


**Figure S21.** Partial density of states (PDOS) analysis for the d-band of different metals.

**Table S1.** Parameters for Fe and Ni K-edge EXAFS for Fe-Ni@ACC and reference samples. ( $S_0^2=0.89$ ).

Sample	Shell	CN	R/Å	$\sigma^2/10^{-3}\text{Å}^2$	$\Delta E$ (eV)	R factor
<b>Fe K-edge</b>	Fe-Ni	8.72±0.64	2.50±0.005	7.41±0.65	5.00±0.72	0.008
	Fe-Fe	6.48±0.44	2.52±0.005	5.05±0.60	6.59±0.67	0.008
<b>Ni K-edge</b>	Ni-Fe	7.04±0.50	2.51±0.005	5.03±0.63	6.61±0.66	0.006
	Ni-Ni	9.65±0.43	2.50±0.003	7.60±0.40	5.08±0.42	0.002

$S_0^2$  is the amplitude reduction factor. CN is the coordination number of neighboring atom. R is the distance to neighboring atom.  $\sigma^2$  is the Debye-Waller factor (Mean-square disorder of neighbor distance).  $\Delta E$  is the energy zero migration (the difference between the zero kinetic energy of the sample and that of theoretical model). R factor is used to value the goodness of the fitting. A reasonable range of EXAFS fitting parameters:  $0.700 < S_0^2 \leq 1.000$ ;  $CN > 0$ ;  $\sigma^2 > 0 \text{ Å}^2$ ;  $\Delta E < 10 \text{ eV}$ ; R factor  $< 0.02$ .

**Table S2.** The thickness of different components of the Zn-I<sub>2</sub> batteries in this work.

Component	Thickness (mm)
Cathode	0.790
Interlayer	0.275
Separator	0.528
Anode	0.1

The volumetric energy density  $E = C * U / V$ , where C denoted the total capacity of the coin cell, U represented the average working voltage, and V stood for the combined volume of the cathode, interlayer, separator and anode, which is estimated based on the total thickness of main components. The volumetric energy density of the Zn-I<sub>2</sub> batteries assembled with no interlayer was 24.70 Wh L<sup>-1</sup>, while that of the Zn-I<sub>2</sub> batteries assembled with the Pristine ACC interlayer was 26.12 Wh L<sup>-1</sup>.

**Table S3.** The cell performance collected from other reported Zn-I<sub>2</sub> batteries.

Modifications	Cycle number	Current density (A g <sup>-1</sup> )	Specific capacity (mAh cm <sup>-2</sup> )	Ref
NiSAs-HPC/I <sub>2</sub>	10000	4.22	0.138	6
B-Fe-NC/I <sub>2</sub>	5000	1	0.18	7
GC-PAN/I <sub>2</sub>	2000	2	0.23	8
HC@FeNC	1000	0.5	0.9	9
Co[Co <sub>1/4</sub> Fe <sub>3/4</sub> (CN) <sub>6</sub> ]/I <sub>2</sub>	2000	4	0.4	10
Ni-N <sub>4</sub> CNF/I <sub>2</sub>	5900	3	0.405	11
PTC interlayer	8500	2	0.35	12
SACu@NKB	1800	2	0.35	13
I <sub>2</sub> @PFC-72-Co	5000	4.2	0.53	14
CC-I <sub>2</sub>	500	1	1.98	15
Dowex+Fe-SCNT/GF	1000	4	2.43	16
AC/CFC	5000	0.2	2.46	17
MX-AB@I	500	1	2.24	18
This work	3000	1	3.27	This work
	12000	4.22	1.3	

## Reference

- 1 G. Kresse and J. Furthmüller, *Phys. Rev. B*, 1996, **54**, 11169–11186.
- 2 G. Kresse and J. Furthmüller, *Comput. Mater. Sci.*, 1996, **6**, 15–50.
- 3 P. E. Blöchl, *Phys. Rev. B*, 1994, **50**, 17953–17979.
- 4 J. P. Perdew, K. Burke and M. Ernzerhof, *Phys. Rev. Lett.*, 1996, **77**, 3865–3868.
- 5 S. Grimme, J. Antony, S. Ehrlich and H. Krieg, *The Journal of Chemical Physics*, 2010, **132**, 154104.
- 6 L. Ma, G. Zhu, Z. Wang, A. Zhu, K. Wu, B. Peng, J. Xu, D. Wang and Z. Jin, *Nano Lett.*, 2023, **23**, 5272–5280.
- 7 M. Liu, Q. Chen, X. Cao, D. Tan, J. Ma and J. Zhang, *J. Am. Chem. Soc.*, 2022, **144**, 21683–21691.
- 8 L. Zhang, M. Zhang, H. Guo, Z. Tian, L. Ge, G. He, J. Huang, J. Wang, T. Liu, I. P. Parkin and F. Lai, *Adv. Sci.*, 2022, **9**, 2105598.
- 9 Y. Wang, X. Jin, J. Xiong, Q. Zhu, Q. Li, R. Wang, J. Li, Y. Fan, Y. Zhao and X. Sun, *Advanced Materials*, 2024, **36**, 2404093.
- 10 L. Ma, Y. Ying, S. Chen, Z. Huang, X. Li, H. Huang and C. Zhi, *Angew. Chem., Int. Ed.*, 2021, **133**, 3835–3842.
- 11 W. Qu, J. Zhu, G. Cao, S. Chen, Y. Tan, B. Chen and M. Zhang, *Small*, 2024, **20**, 2310475.
- 12 Y. Zhang, T. Zhao, S. Yang, Y. Zhang, Y. Ma and Z. Wang, *J. Energy Chem.*, 2022, **75**, 310–320.
- 13 F. Yang, J. Long, J. A. Yuwono, H. Fei, Y. Fan, P. Li, J. Zou, J. Hao, S. Liu, G. Liang, Y. Lyu, X. Zheng, S. Zhao, K. Davey and Z. Guo, *Energy Environ. Sci.*, 2023, **16**, 4630–4640.
- 14 C. Guo, Y. Cao, Y. Gao, C. Zhi, Y. Wang, Y. Luo, X. Yang and X. Luo, *Adv. Funct. Mater.*, 2024, **34**, 2314189.
- 15 S. Lv, T. Fang, Z. Ding, Y. Wang, H. Jiang, C. Wei, D. Zhou, X. Tang and X. Liu, *ACS Nano*, 2022, **16**, 20389–20399.
- 16 Y. Kang, G. Chen, H. Hua, M. Zhang, J. Yang, P. Lin, H. Yang, Z. Lv, Q. Wu, J. Zhao and Y. Yang, *Angew. Chem., Int. Ed.*, 2023, **62**, e202300418.
- 17 Y. Yang, S. Liang, B. Lu and J. Zhou, *Energy Environ. Sci.*, 2022, **15**, 1192–1200.
- 18 D. Li, Y. Zhu, L. Cheng, S. Xie, H. Yu, W. Zhang, Z. Xu, M. Ma and H. Li, *Adv. Energy Mater.*, 2024, 2404426.